Gust Response Predictions of a Very Flexible Wing Model

Stefanie Düssler*
Pilatus Aircraft, Ltd., 6371 Stans, Switzerland
Christoph Mertens†
Royal Netherlands Aerospace Centre, 1059 CM Amsterdam, The Netherlands
and
Rafael Palacios‡
Imperial College, London, England SW7 2AZ, United Kingdom

https://doi.org/10.2514/1.C038332

Nonlinear aeroelastic simulations are benchmarked against wind tunnel experiments of a very flexible wing. In the simulations, sectional force corrections are employed to capture low-Reynolds-number effects and the static lift deficiency due to the onset of flow separation. With these corrections, both the static and dynamic wing deformation predictions match the experiments well (2% and 6% error, respectively). Furthermore, a simulation of the unsteady inflow to the Delft-Pazy wing that is produced by the gust vanes in the wind tunnel is explored as an alternative to a frozen gust model. Results indicate a considerable influence of the wing's presence on the gust velocity that was measured upstream of the wing in the wind tunnel experiment. The structural response, however, differs only slightly when using the two different gust models. This confirms that the uniform gust is still a valid assumption for moderately large deflections (up to 24% of the wingspan in this work). Finally, geometrically nonlinear effects are assessed and found to be relevant in the simulations because of the nonlinear aeroelastic equilibrium, but not because of the gust excitation.

Nomenclature

$\boldsymbol{A}, \boldsymbol{B}, \boldsymbol{C}, \boldsymbol{D}$ = state, input, output, and feed-through matrices
$\boldsymbol{\mathcal{A}}$ = aerodynamic influence coefficient matrix
B, S = body-attached and local structural frames of reference
b = half-wing span, m
$\boldsymbol{\mathcal{C}}$ = constant, tangential damping matrix
c = chord length, m
c_l = airfoil lift coefficient
d_h, d_v = horizontal and vertical gust vane distance, m
$\boldsymbol{F}$ = dimensionless forces
f = frequency, Hz
$\boldsymbol{f}$ = structural force vector, N
$\boldsymbol{\mathcal{K}}$ = constant, tangential stiffness matrix
k = reduced frequency
$\boldsymbol{\mathcal{M}}$ = mass matrix
$\boldsymbol{m}$ = structural moment vector, $\mathrm{N} \cdot \mathrm{m}$
$\bar{m}$ = distributed mass, m/kg
$\boldsymbol{\mathcal{N}}$ = force matrix
$\boldsymbol{q}$ = modal displacement
$\boldsymbol{\mathcal{R}}$ = coordinate transformation matrix
Re = Reynolds number
$\boldsymbol{r}$ = position vector, m
T = time period, s
t = time, s
$\boldsymbol{U}$ = flow velocity, m/s
$\boldsymbol{u}$ = induced velocity, m/s
w = wingtip deflection, m
$\boldsymbol{w}_g$ = gust velocity input, m/s
α = angle of attack, deg
$\boldsymbol{\Gamma}$ = circulation strengths
δ = gust vane deflection, deg
ϵ = relative error, %
$\boldsymbol{\zeta}$ = lifting surface lattice coordinates
$\boldsymbol{\eta}$ = displacement and rotation vector
ν, ζ = spanwise and streamwise curvilinear wake coordinates
$\boldsymbol{\xi}$ = structural nodes displacement vector
$\boldsymbol{\Phi}$ = modal projection matrix

I. Introduction

FUTURE transport aircraft are expected to have much higher-aspect-ratio wings, resulting in higher flexibility, and thus larger deformation. The question arises: Which simulation methods can sufficiently predict the resulting aeroelastic and possible nonlinear dynamics while still being computationally affordable? This topic has recently been addressed in the Large Deflection Working Group,§ part of the Third Aeroelastic Prediction Workshop, in the context of flutter prediction [1]. The focus of the group's activity has been on the *Pazy wing*, a very flexible benchmark experimental model, designed and tested at the Technion [2,3]. An additional relevant area of research arises from the fact that the structural dynamic characteristics and aerodynamic features of very flexible wing structures, such as the Pazy wing, can also change significantly in the event of strong gust-induced deformation [4].

In this context, Ref. [5] presents a slightly altered design of the Pazy wing, with the same external dimensions but an even higher flexibility, which was tested in a low-speed wind tunnel facility equipped with a gust generator at Delft University of Technology and is henceforth referred to as the *Delft-Pazy wing*. Their focus has been on characterizing periodic gust responses experimentally using nonintrusive measurements of the flowfield and the structural deformations, using a method-based volumetric particle tracking velocimetry [6]. The periodic gust was generated in the wind tunnel with two oscillating gust vanes upstream of the wing. The accurate experimental characterization of such a gust inflow is sometimes not trivial due to the interaction of the

---

Received 21 January 2025; accepted for publication 21 May 2025; published online 31 July 2025. Copyright © 2025 by Stefanie Düssler, Cristoph Mertens and Rafael Palacios. Published by the American Institute of Aeronautics and Astronautics, Inc., with permission. All requests for copying and permission to reprint should be submitted to CCC at www.copyright.com; employ the eISSN 1533-3868 to initiate your request. See also AIAA Rights and Permissions https://aiaa.org/publications/publish-with-aiaa/rights-and-permissions/.

*Loads & Aeroelastics Engineer; formerly Ph.D. Candidate, Imperial College London.

†R&D Engineer, Flight Test and Certification Department; christoph.mertens@nlr.nl; formerly Ph.D. Candidate, The Delft University of Technology.

‡Professor of Computational Aeroelasticity, Department of Aeronautics; r.palacios@imperial.ac.uk. Associate Fellow AIAA.

§Data available online at https://nescacademy.nasa.gov/workshops/AePW3/public/wg/largedeflection.

gust with the highly deformed experimental model that is being tested and other experimental setup components that alter the inflow with respect to an undisturbed flow. To characterize the gust that was realized in the wind tunnel experiment of the Delft-Pazy wing, the inflow velocity variation has been analyzed at only 0.75 chord lengths upstream of the wing in Ref. [5]. In Ref. [7], a validation of a three-dimensional free wake panel method has been obtained using these experiments, the results of which gave rise to the suspicion of an erroneous measurement of the gust velocity magnitude and a phase shift due to the influence of the unsteady wing motion on the inflow velocity at the selected gust inflow measurement location.

In this study, we aim to further investigate this hypothesis by modeling the gust itself, simulating the oscillating gust vanes and their shed wakes representing the gust using the aeroelastic simulation toolbox `SHARPy`. This gust vane modeling has previously been performed using the unsteady vortex lattice method (UVLM) in Ref. [8], which also compared the resulting induced gust velocities to simplified, two-dimensional computational fluid dynamics (CFD) simulations [9]. For the present study, we model not only the gust vanes but also simultaneously the unsteady aeroelastic response of the Delft-Pazy wing. This approach allows us to explore potential limitations of the frozen gust assumption and assess the modeling requirements for the nonlinear aeroelastic simulation of gust response.

The paper is structured such that we introduce the numerical methods used for the fully nonlinear aeroelastic simulations and for the linearization and order-reduction process in Sec. II. Next, the Delft-Pazy wing and the experimental setup are briefly introduced, followed by a description of the computational implementation (Sec. III). In Sec. IV, we evaluate the frozen gust response prediction capabilities of the nonlinear aeroelastic solver by comparing it against the experimental results. Subsequently, we discuss the results obtained when modeling both the Delft-Pazy wing and the gust vanes by evaluating the induced velocity field and the dynamic wing deformation response in Sec. V. We finally evaluate the relevance of nonlinear structural effects in the simulations in Sec. VI.

II. Aeroelastic Computational Methods

The nonlinear aeroelastic simulations are performed with the open-source simulation environment `SHARPy` [10]. `SHARPy` couples a nonlinear, displacement-based, geometrically exact composite beam model (GEBM) and UVLM for the aerodynamics. In this section, we briefly introduce the nonlinear solver, with emphasis on the force corrections, followed by some details of the linearized solver against which the dynamic results will be benchmarked.

A. Nonlinear Aeroelastic Solver

1. Structural Dynamics

The primary structure of the wing is modeled by geometrically nonlinear beams discretized in quadratic (3-node) finite elements [11,12] written in terms of the nodal displacements and rotations, denoted by $\boldsymbol{\eta}$. The local rotation is determined by the orientation of the frame of reference (FoR) S, which is attached to the node and moves with it, with respect to a global frame B at the wing root. Both are shown schematically in Fig. 1. The corresponding coordinate transformation matrix is $\boldsymbol{\mathcal{R}}^{\mathrm{SB}}$.

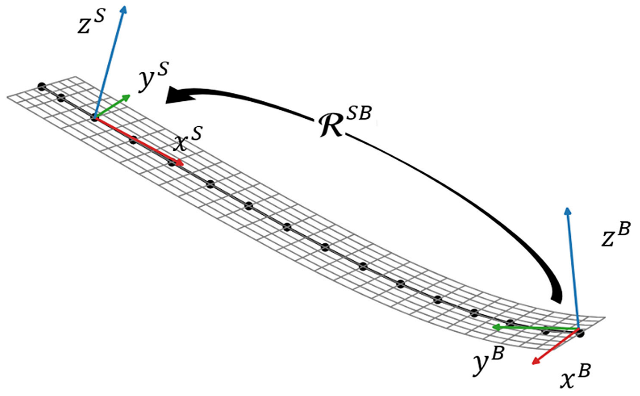

Fig. 1 Illustration of the frames of reference as well as a typical structural and aerodynamic model of a rectangular wing.

Hamilton's principle is then used to describe the beam dynamics, whose nonlinear form is [13]

$$\boldsymbol{\mathcal{M}}(\boldsymbol{\eta})\ddot{\boldsymbol{\eta}} + \boldsymbol{\mathcal{N}}_{\mathrm{gyr}}(\boldsymbol{\eta}, \dot{\boldsymbol{\eta}}) + \boldsymbol{\mathcal{N}}_{\mathrm{stiff}}(\boldsymbol{\eta}) = \boldsymbol{\mathcal{N}}_{\mathrm{ext}}(\boldsymbol{\eta}, \dot{\boldsymbol{\eta}}) \tag{1}$$

with the mass matrix $\boldsymbol{\mathcal{M}}$ and gyroscopic, stiffness, and external generalized forces $\boldsymbol{\mathcal{N}}$. Both the inertial and elastic forces are nonlinear in Eq. (1), which is solved iteratively with a Newton–Raphson scheme, while an explicit, incrementally formulated Newmark-β scheme [14] is used for the time integration.

2. Unsteady Aerodynamics

The aerodynamic loads are given by the UVLM, which captures unsteady effects on low-speed attached flows over thin lifting surfaces [15]. The UVLM is strongly coupled to the structural solver at each time step, and the resulting loads are applied as follower forces on the beam structure. Aerodynamic surfaces are discretized using a lattice of quadrilateral panels, whose corner points' coordinates are aggregated into a column matrix $\boldsymbol{\zeta}(t)$. Each panel is associated with a bound vortex ring (index b) with a circulation, denoted by $\boldsymbol{\Gamma}_b$. Another grid of unbound vortex rings captures the wake (index w), which is formed from vortices shed to satisfy the Kutta–Joukowsky condition at the trailing edge [16].

A *horseshoe wake* model is used for steady aeroelastic analysis, while both prescribed and free wake convection schemes have been implemented for unsteady problems. The last two are illustrated in Fig. 2. In the prescribed wake model, the vortex rings on the wake move with the combination of the freestream and the gust velocities (the *background flowfield*). In the free wake model, the local velocity induced at every instant by the vortex lattice is also included, so as to capture wake roll-up. This approach, however, involves considerable additional computational costs.

Once the geometry is established and the singularity elements are positioned on both the lifting surface and wake panels, the induced velocity field at an arbitrary point in space $\boldsymbol{r}$ can be computed from

$$\boldsymbol{u}(\boldsymbol{r}, t) = \boldsymbol{\mathcal{A}}_b(\boldsymbol{r}, \boldsymbol{\zeta}(t))\boldsymbol{\Gamma}_{\boldsymbol{b}}(t) + \boldsymbol{\mathcal{A}}_w(\boldsymbol{r}, \boldsymbol{\zeta}(t))\boldsymbol{\Gamma}_{\boldsymbol{w}}(t) \tag{2}$$

with $\boldsymbol{\mathcal{A}}_b$ and $\boldsymbol{\mathcal{A}}_w$ the aerodynamic influence coefficient (AIC) matrices, which are calculated using Biot–Savart law. Enforcing nonpenetrating boundary conditions at collocation points on the panels defines sufficient conditions to determine the bound circulation. For symmetric models, we enforce equal circulation on pairs of symmetric surfaces, thus reducing the system to half the size.

The instantaneous geometry of the wake is described by curvilinear coordinates along spanwise and streamwise directions. Convection of circulation only occurs along the streamwise coordinate ξ, according to

$$\frac{\Gamma_\xi^{t+1} - \Gamma_\xi^t}{\Delta t} + u_r \frac{\Gamma_\xi^t - \Gamma_{\xi-1}^t}{\Delta \xi} = 0 \tag{3}$$

using a first-order upwind discretization. In this equation, $\Delta\xi$ is the vortex size in the streamwise direction, and u_r is the relative flow-solid velocity. Panel methods commonly use a Courant–Friedrichs–Lewy number $\mathrm{CFL} \coloneqq u_r \Delta t / \Delta\xi$ of one [17]. In the current formulation, this is enforced by determining the chordwise length of each newly shed wake vortex from the time step, establishing a connection between spatial and temporal discretization as $\Delta t = c/(M \cdot U_\infty)$, where c is the chord length. As a result, a finer discretization with M panels in the chordwise direction requires a smaller time step. This results in more panels in the chordwise direction for the same physical length of the wake. Furthermore, with a fixed time step but different-sized lifting surfaces (as is the case in this work with the simultaneous simulation of the gust vanes and the Delft-Pazy wing), it is important to adjust the chordwise

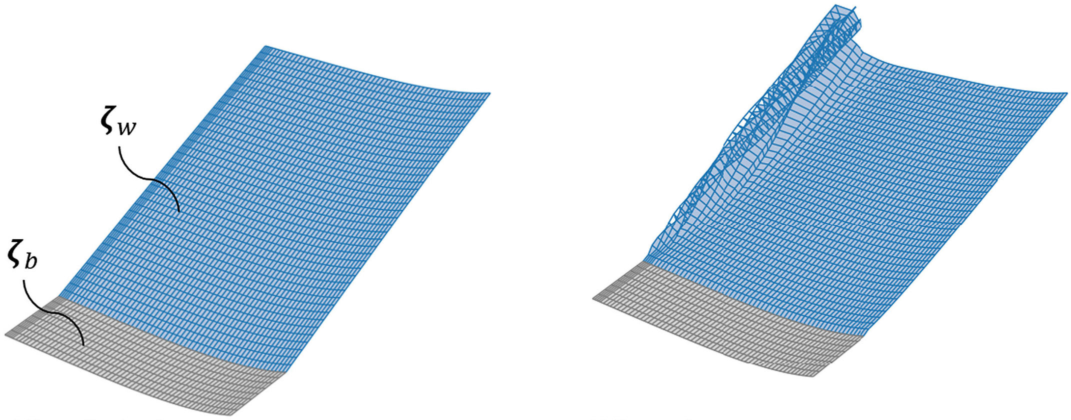

a) Prescribed wake **b) Free wake**

Fig. 2 Symmetric cantilever wing with illustrated wake resulting from different wake convection schemes.

discretization of these surfaces such that the condition CFL $= 1$ is satisfied for all surfaces.

3. Aerodynamic Force Computations and Sectional Correction

We compute the instantaneous aerodynamic forces on the structure from the bound circulation, $\boldsymbol{\Gamma}_b$. Vortex rings induce a quasi-stationary force that takes into account the leading-edge suction and can be calculated at each vortex segment center using Joukowsky's theorem. The noncirculatory forces are obtained at the center of each vortex ring from the added mass contribution in Bernoulli's principle [18]. Both force contributions are then linearly interpolated to the corners of the vortex rings $\boldsymbol{\zeta}$, integrated along the chord into sectional loads, and finally applied as follower forces and moments on the nodes of the discrete (beam) structure. If S is the local material frame at the node i (see Fig. 1), the resultant aerodynamic forces and moments at that node will be denoted by $\boldsymbol{f}_S^{(i)}$ and $\boldsymbol{m}_S^{(i)}$, respectively.

Finally, adjustment of the lift curve slopes, including thickness, viscous effects, and static lift deficiency for higher angles of attack at the onset of stall, is done with the sectional force correction method that was presented and validated in Ref. [19]. This approach consists of three steps:

1) The relative velocity between the flow and the moving structure is computed at node i and written in coordinates in the Earth reference frame G, namely, $\boldsymbol{u}_{\mathrm{rel},G}^{(i)}$. The average flow velocity at the section is considered. Note that for this problem the G frame differs from the B frame in Fig. 1 by the angle of incidence of the wing.

2) Compute the sectional lift coefficient $c_l^{(i)}$ from the component nodal force in the normal direction to $\boldsymbol{u}_{\mathrm{rel},G}^{(i)}$, normalized by $(1/2)\rho\|\boldsymbol{u}_{\mathrm{rel},G}^{(i)}\|A^{(i)}$, with $A^{(i)}$ the surface area between two spanwise nodes.

3) Compute the effective sectional angle of attack (which now considers complex dynamics and large deformations) from the local section, as $\alpha_e = (c_l^{(i)}/2\pi) + \alpha_0$, where α_0 is the zero-lift angle associated with the local camber of the UVLM section, and 2π refers to the curve slope in potential flow.

4) The corrected sectional forces and moments are finally obtained from the airfoil polar with α_e and the instantaneous relative speed $\|\boldsymbol{u}_{\mathrm{rel},G}^{(i)}\|$. We replace the nodal forces in the lift and drag directions, as well as the pitching moment, using this approach.

Alternatively, if only the lift curve slope is corrected, the resulting sectional forces and moments can also just be multiplied by a user-specified factor. Either correction is applied within the fluid–structure interaction (FSI) loop before passing the forces $\boldsymbol{f}_S^{(i)}$ and moments $\boldsymbol{m}_S^{(i)}$ to the structural subsystem.

B. Linearization Process

A linear model will be used as a reference for the transient results. Linearization is performed individually for the UVLM and GEBM around the nonlinear aeroelastic equilibrium of the system, which is denoted by the subscript $(\cdot)_0$ and is computed using the methods of Sec. II.A. At this equilibrium, velocities and accelerations are identically zero, and the external forces must be in balance with the stiffness forces, i.e., $\boldsymbol{N}_{\mathrm{stiff}}(\boldsymbol{\eta}) = \boldsymbol{N}_{\mathrm{ext}}(\boldsymbol{\eta}, \dot{\boldsymbol{\eta}})$, from which we can derive the tangential stiffness matrices, denoted by $\boldsymbol{\mathcal{K}}$. With these conditions for the equilibrium state, we can perturb the GEBM model from Eq. (1), assuming small amplitudes, resulting in

$$\boldsymbol{\mathcal{M}}(\boldsymbol{\eta}_0)\Delta\ddot{\boldsymbol{\eta}} + \boldsymbol{\mathcal{K}}(\boldsymbol{\eta}_0)\Delta\boldsymbol{\eta} = \Delta\boldsymbol{\mathcal{N}}_{\mathrm{ext}}(\Delta\boldsymbol{\eta}, \Delta\dot{\boldsymbol{\eta}}) \tag{4}$$

Here, $\Delta(\cdot)$ denotes small perturbations around the reference, and the state variables consist of the flexible degree of freedom (DoF) deviations $\Delta\boldsymbol{\eta}_i$ for each node i and their gradient $\Delta\dot{\boldsymbol{\eta}}_i$. We further reduce the linear structural system by projecting it onto the modal coordinates of the deformed system and truncating it to a suitable number of modes that capture the most important dynamics. More precisely, this modal projection, expressed as $\Delta\boldsymbol{\eta} = \boldsymbol{\Phi}\Delta\boldsymbol{q}$ and $\Delta\dot{\boldsymbol{\eta}} = \boldsymbol{\Phi}\Delta\dot{\boldsymbol{q}}$, is obtained by calculating $\boldsymbol{\Phi}$ from the solution of the eigenvalue problem by inserting Eq. (4) into the above equations. The modal displacement field $\boldsymbol{q}$ and the resulting modal velocities $\dot{\boldsymbol{q}}$ then describe the structural dynamics.

Subsequently, we analytically linearize the UVLM with the assumption of constant AICs and a frozen wake shape, while including steady load effects. This yields a discrete, linear time-invariant (DLTI) system in state-space [20]. The gust inputs, which map three-dimensional velocity vectors to each vortex-ring panel leading to a high number of inputs, have been reduced to a single gust input $\boldsymbol{w}_g$ as described in Ref. [13]. This input characterizes the vertical velocity at the foremost leading edge and maps it with the states $\boldsymbol{x}_{w_g}$ across the lattice grid points $\boldsymbol{\zeta}$. This mapping is based on a linear interpolation approach while considering a convection of this gust velocity downstream with the freestream velocity (as does any disturbance in the UVLM). The augmented DLTI-UVLM can then be written as

$$\boldsymbol{x}_a(k+1) = \boldsymbol{A}_a\boldsymbol{x}_a(k) + \boldsymbol{B}_a\boldsymbol{u}_a(k) \tag{5}$$

$$\boldsymbol{y}_a(k) = \boldsymbol{C}_a\boldsymbol{x}_a(k) + \boldsymbol{D}_a\boldsymbol{u}_a(k) \tag{6}$$

with the states $\boldsymbol{x}_a(k) = [\Delta\boldsymbol{x}_{w_g}, \Delta\boldsymbol{\Gamma}_b, \Delta\boldsymbol{\Gamma}_w, h\Delta\dot{\boldsymbol{\Gamma}}_b, \Delta\boldsymbol{\Gamma}_b(k-1)]$, and the output is composed of the dimensionless forces, including steady and unsteady components, at these vertices, and is written as $\boldsymbol{y}_a(k) = \Delta\boldsymbol{F}(k)$. The inputs are $\boldsymbol{u}_a(k) = [\Delta\boldsymbol{\zeta}, \Delta\dot{\boldsymbol{\zeta}}, \Delta\boldsymbol{w}_g]$. The integers k and h are the current discrete time step and its size. To improve readability, we omit specifying the discrete time step of an aeroelastic parameter if referring to the current time step. We capture the added mass effects with the time derivative $\dot{\boldsymbol{\Gamma}}_b$, computed with second-order accuracy (thus $\Delta\boldsymbol{\Gamma}_b(k-1)$ is also a state).

To couple the aerodynamic and structural dynamic systems, the aerodynamic force output $\Delta\boldsymbol{F}$ stemming from the DLTI-UVLM system in the B-frame is projected onto the structural DoF in the

S-frame. These transformed forces can then be input directly into the GEBM system as forces and moments using linear mapping. The GEBM system then yields the resulting grid geometries and velocities based on the subsequent node displacements and velocities, which then serve as inputs to the DLTI UVLM system. The resulting linearized coupled aeroelastic system

$$\begin{aligned} \boldsymbol{x}_{ae}(k+1) &= \boldsymbol{A}_{ae}\boldsymbol{x}_{ae}(k) + \boldsymbol{B}_{ae}\boldsymbol{u}_{ae}(k) \\ \boldsymbol{y}_{ae}(k) &= \boldsymbol{C}_{ae}\boldsymbol{x}_{ae}(k) + \boldsymbol{D}_{ae}\boldsymbol{u}_{ae}(k) \end{aligned} \tag{7}$$

has now the input $\boldsymbol{u}_{ae}(k) = \Delta\boldsymbol{w}_g$, and the following states and outputs for the linear full-order model (FOM) system:

$$\boldsymbol{x}_{ae}(k) = [\Delta\boldsymbol{x}_{w_g}, \Delta\boldsymbol{\Gamma}_b, \Delta\boldsymbol{\Gamma}_w, h\Delta\dot{\boldsymbol{\Gamma}}_b, \Delta\boldsymbol{\Gamma}_b(k-1), \Delta\boldsymbol{q}, \Delta\dot{\boldsymbol{q}}]$$

$$\boldsymbol{y}_{ae}(k) = [\Delta\boldsymbol{\mathcal{N}}, \Delta\boldsymbol{\eta}, \Delta\dot{\boldsymbol{\eta}}]$$

Here, $\Delta\boldsymbol{\mathcal{N}}$ denotes the structural forces and moments.

III. Delft-Pazy Wing Design, Experiments, and Computational Model

A. Delft-Pazy Wing Design and Ground Vibration Test

The Delft-Pazy wing wind tunnel model design is mostly identical to the Pazy wing that is described in detail in Ref. [2]. This unswept and untapered wing has a chord length of $c = 100$ mm and a span width of $b = 550$ mm. The main difference between the original Pazy wing and the Delft-Pazy wing is a reduced thickness of the inner spar plate made from aluminum, which is 1.5 mm for the Delft-Pazy wing instead of 2.25 mm for the original Pazy wing. This modification has been implemented to produce comparably large deformations to those observed on the Pazy wing at the Technion at freestream velocities up to $U_\infty = 55$ m/s in a low-speed wind tunnel facility at Delft University of Technology at only $U_\infty = 18.3$ m/s. Furthermore, the outer surface of the Delft-Pazy wing is covered with nonreflective black paint to facilitate optical flowfield measurements in the wind tunnel. On this coating, a pattern of white circular reflective markers is applied for tracking the structural motion of the wing, as shown in Fig. 3.

To characterize the structural behavior of the Delft-Pazy wing, a ground vibration test (GVT) was performed before the wind tunnel experiment. The GVT is performed using a modal hammer and a laser scanning vibrometer. More details about the wing design and the GVT are provided in Ref. [5]. The GVT results provide the first five experimental mode shapes and frequencies, these are included in the later discussed Table 2.

B. Wind Tunnel Experiment

The wind tunnel experiment was performed at the Open Jet Facility (OJF) at the Delft University of Technology. The OJF is a closed-loop, open test section wind tunnel with an octagonal outlet spanning 2.85 m by 2.85 m, which was operated at a freestream velocity of 18.3 m/s. A photograph of the wind tunnel setup with an indication of the relevant components is shown in Fig. 4.

Upstream of the wing, at a streamwise horizontal distance of approximately $d_h = 1.5$ m from the Delft-Pazy wing that is placed at the center of the test section, are the two vertical gust vanes, which are operated in a continuous sinusoidal pitching motion during the tests. The Delft-Pazy wing itself is mounted vertically on a six-component balance. On the right side in the photograph in Fig. 4, the optical measurement setup is visible. The main objective of the wind tunnel experiment was the development of an aeroelastic characterization approach that describes the unsteady loads acting on the wing based on nonintrusive measurements with this optical setup, as described in detail in Ref. [5]. For the purpose of the present study, the focus is placed on the structural response of the wing to the periodic gust excitation, and therefore the measurement of both of these is described in the following.

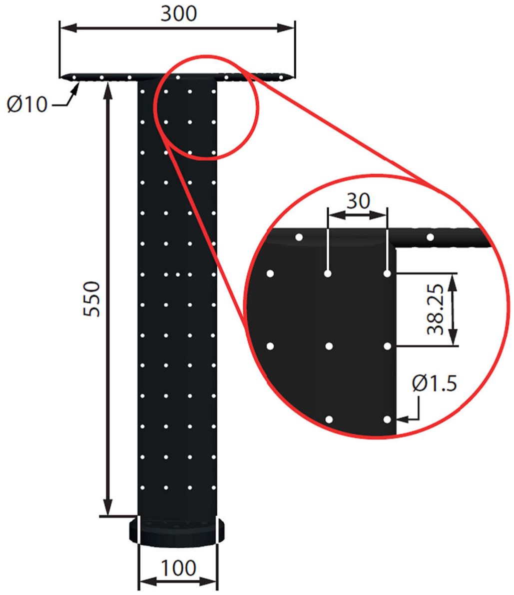

Fig. 3 Sketch of the Delft-Pazy wing. Dimensions are in mm.

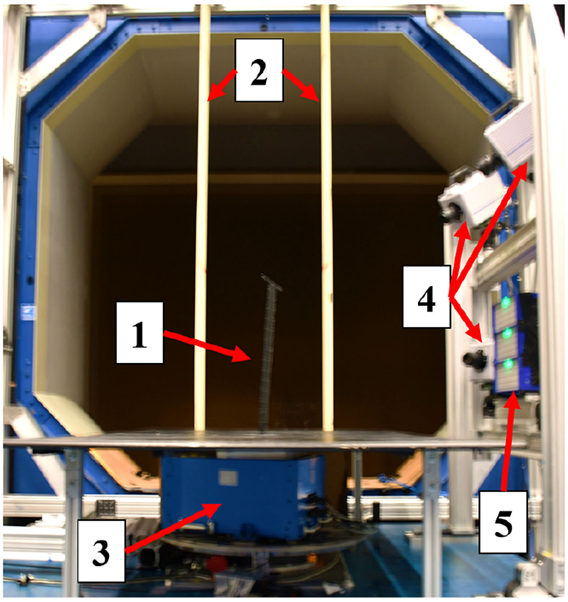

Fig. 4 Wind tunnel setup in the OJF, looking upstream. 1: Delft-Pazy wing; 2: gust generator vanes; 3: six-component balance; 4: 3× high speed cameras; 5: 3× LED units.

The structural response of the wing is measured experimentally by tracking the markers on the surface with the same optical measurement system (which is conventionally only used for flowfield measurements) in an integrated measurement approach, which was introduced first in Ref. [21]. Due to limitations of the measurement volume size of this system, several measurements of the structural response in terms of the marker displacements at different locations of the wing were combined into one data set and subsequently analyzed in a phase-averaged approach. In this approach, a sinusoidal fit was performed for the periodic displacement per marker, and afterward, the wing shape was reconstructed to best fit these measurements based on a polynomial fit of the spanwise central axis of the wing. Torsional deformations were analyzed and considered small enough in the experiments to be neglected for the considered test cases. The wing deformation is thus described solely in terms of the out-of-plane bending and can therefore be summarized in terms of a mean tip deflection w, a dynamic tip deflection amplitude $\hat{w}$, and a phase lag Φ of the dynamic wing motion with respect to the incoming gust (see Table 1).

Table 1 Overview of the dynamic wind tunnel test conditions and wing deflection results

Test case	Angle of attack α, deg	Static tip deflection w/b, %	Gust frequency f_g, Hz	Tip deflection amplitude $\hat{w}/b$, %	Phase shift to incoming gust Φ, deg	Measured gust amplitude A_g, $\mathrm{m \cdot s^{-1}}$
1	5	8.5	5.7	1.8	−171	0.81
2	10	15.9	3.2	8.2	+99	0.65

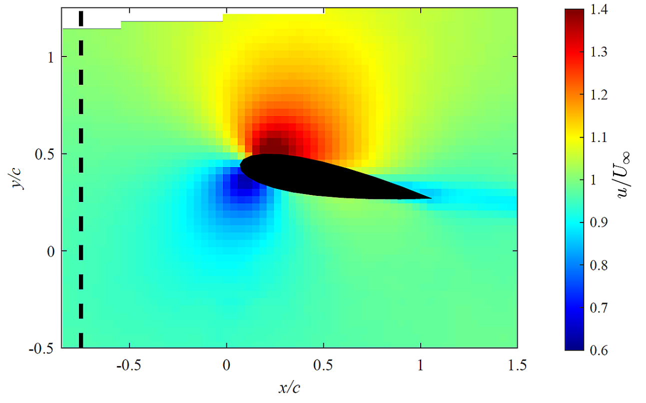

Fig. 5 Measured flow velocity at midspan during the upstroke of the wing motion in test case 2. Dashed line shows location for gust extraction; origin at the undeformed wing leading edge.

The phase and amplitude of the incoming gust are determined experimentally based on the phase-averaged flowfield measurements in the wind tunnel. This is achieved by analyzing the variation in the transversal velocity component upstream of the wing at $x = -0.75c$ (see Fig. 5). This location has been selected because it is near the upstream edge of the measurement volume, where flowfield information is available. Measurements further upstream would be desirable to further reduce the effect of the presence of the wing on the gust velocity measurement but could not be realized in the experimental campaign. At the selected location, the transversal velocity component exhibits a nearly ideal sinusoidal behavior, which permits the quantification of the phase and angle and gust amplitude as given in Table 1. More details about the flowfield measurements and data processing can be found in Ref. [5].

C. Computational Model Implementation

A numerical model of the Delft-Pazy wing is implemented into `SHARPy`, where the aerodynamic lifting surfaces are modeled using a flat plate of vortex panels. The cantilever wing is simulated with a symmetry condition applied at the root. The beam is discretized into 30 three-noded elements, resulting in 61 spanwise vortex ring panels on the lifting surface. In the chordwise direction, eight vortex ring panels are employed. The topology is identical to that of Fig. 1, other than with a different aspect ratio.

The main sectional structural stiffness and mass properties along the wing are shown in Fig. 6 and are derived from Ref. [22]. Similar methodologies have been employed previously to construct an equivalent beam model for the Pazy wing using the Enhanced FEM2Stick (EF2S) framework, as described in Ref. [23]. This EF2S framework, which is employed in the present work as well, assumes infinite shear stiffness.

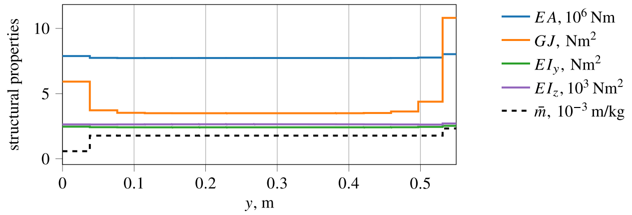

Fig. 6 Sectional structural stiffness and mass distribution of the beam model.

The modal frequencies of `SHARPy`'s Delft-Pazy model under unloaded conditions are compared with the frequencies obtained from the GVT as well as the finite element Nastran model used in the EF2S to create the beam model. The results are shown in Table 2. Between the finite element model and `SHARPy`, we observe an excellent agreement, where the maximum relative error is just above 1% for the first five modes. The second torsional mode, which, however, has a very high frequency and is less crucial for the aeroelastic dynamics, differs by 6.14%. The frequencies of the Delft-Pazy wing wind tunnel model measured in the GVT differ slightly from the finite element model (and thus `SHARPy`), with the relative deviation defined as $\epsilon(f_1, f_2) = (f_2 - f_1)/f_2$ being in reasonable ranges for GVT measurements [5]. Note that the in-plane bending mode could not be captured experimentally with the selected GVT setup but has been found to be important in nonlinear flutter studies [24].

IV. Gust-Induced Wing Deformation Prediction

The capabilities of the nonlinear aeroelastic solver are exercised in this section to compute the steady and gust-induced dynamic deformations of the Delft-Pazy wing, with the experimental results serving as a reference. For the steady results, horseshoe vertices model the wake. For the dynamic computations, a wake length of $20c$ is chosen, and the prescribed gust convection model is used as the deformation difference to the results using a free wake model are negligibly small (<0.2%). This discretization shows good convergence for both the structure and aerodynamics.

A. Steady Results

We start by computing the steady deformation of the Delft-Pazy wing under the given wind tunnel freestream conditions with a Reynolds number of $Re = 122{,}000$. The lift curve of the NACA0018 airfoil for this Reynolds number is obtained with XFOIL[¶] and shown in Fig. 7. At low angles of attack (below 2.3 deg), this lift curve has a slope of $1.25 \cdot 2\pi$. At $\alpha = 2.3$ deg, the lift curve features a small kink and continues with a higher slope. From around $\alpha = 5.4$ deg onward, flow separation for this airfoil becomes increasingly important [25], which gets compounded with the local shape distortion of the very flexible structure [26]. Sectional drag and moment forces were also computed, but they have a negligible effect on the aeroelastic analysis in this paper.

These conditions must be incorporated in the nonlinear aeroelastic simulation to expect realistic prediction of the aerodynamic forces. This can be achieved with either a constant correction of the lift curve slope c_{l_α} by a factor of 1.25 for lower angles of attack or the described sectional force correction, using this lift curve as an input. The resulting wing deformations are illustrated in Fig. 8 and compared with the experimental deformations for the angles of attack of $\alpha = 5$ deg and $\alpha = 10$ deg investigated in the wind tunnel.

Without the force correction, the wing deformation is underestimated in the nonlinear aeroelastic simulation for both angles of attack. The tip deformation in that case deviates by −14.19% and −11.40% for $\alpha = 5$ deg and $\alpha = 10$ deg, respectively. The c_{l_α} correction results in an almost matching deformation prediction for $\alpha = 5$ deg, but the polar corrections result in an overestimation, both resulting in reduced wing tip displacement errors of 0.96% and 13.05%. These different performances likely stem from deviations of the sectional lift curve obtained from XFOIL and the actual

---

[¶] Data available online at https://web.mit.edu/drela/Public/web/xfoil.

Table 2 Comparison of the modal frequencies

Mode	Description	f_{GVT}, Hz	f_{FEM}, Hz	f_{SHARPy}, Hz	$\epsilon(f_{\mathrm{GVT}}, f_{\mathrm{FEM}})$, %	$\epsilon(f_{\mathrm{FEM}}, f_{\mathrm{SHARPy}})$, %
1	OOP1	3.21	3.43	3.45	6.83	0.58
2	OOP2	22.47	22.81	23.12	1.51	1.36
3	T1	29.49	31.29	31.26	6.10	−0.10
4	OOP3	64.99	65.85	66.54	1.32	1.05
5	IP1	n.a.	106.29	107.40	n.a.	1.04
6	T2	119.70	118.25 Hz	125.50	−1.21	6.13

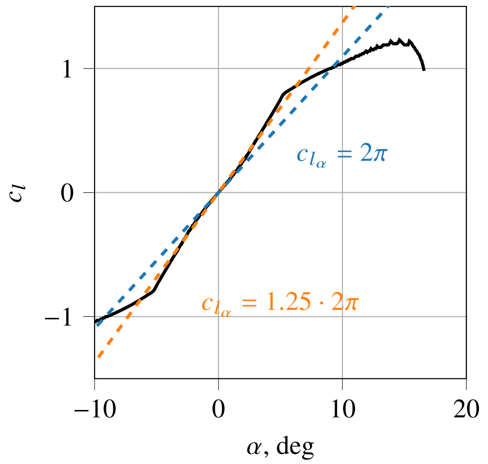

Fig. 7 Lift curve of the NACA0018 airfoil computed with XFOIL for *Re* = 122,000.

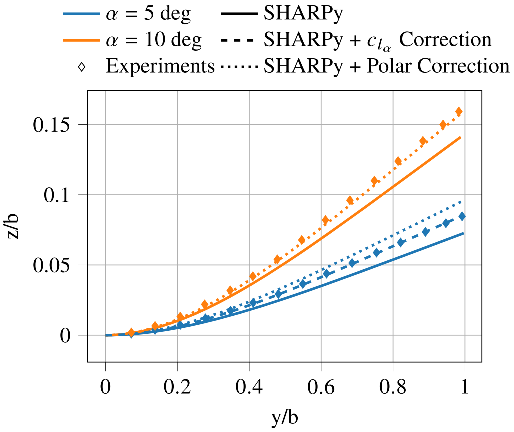

Fig. 8 Steady wing deformation prediction of the Delft-Pazy wing.

experimental one, which is further subject to different wind tunnel blockage effects at different wing deflections. Note also that the nylon cover between the ribs of the wing deforms as the wing bends, which alters the airfoil shape and its aerodynamic properties [26], and even suffers some wrinkling under high compression that may slightly change the local stiffness. For $\alpha = 10$ deg, the polar correction reduces the error in wingtip displacement to -1.38%.

B. Dynamic Results

We continue with presenting the dynamic gust response prediction of the Delft-Pazy wing for the two conditions summarized in Table 1. The same force corrections as in the steady computations are used for each case. The measured gust input from the experiments is used as a frozen gust input to the nonlinear aeroelastic solver in the form of a periodical time series. The solver then maps the gust velocities to the vortex ring collocation points and wake lattice grid points for the aerodynamic solution.

The resulting gust-induced vertical wing deformation at $y/b = 0.9$ for both cases is shown in Fig. 9. The results are obtained from the linear FOM without force correction as well as the nonlinear FOM with and without force correction. For case 1, the initial induced wing vibration indicates an excitation of various modes. The wing oscillations start to converge after 1.2 s with the wing displacement being smaller than the initial response. For case 2, the gust frequency is close to the modal frequency corresponding with the first OOP bending mode. Hence, the gusts excite this mode dominantly, which is seen in the initial response and also in the higher vertical wing displacement amplitudes, resulting in the converged oscillations. Uniform converged oscillation set in for this case after around 1.6 s.

A comparison of the linear and nonlinear FOM without force correction shows a slightly higher deflection amplitude for case 1, which is calculated by the linear FOM at the initial deformation phase. After convergence, the amplitudes become smaller, and there is no longer any difference, which indicates a linear response of the converged oscillation. For case 2, the linear FOM predicts smaller oscillation amplitudes from the beginning. This difference increases for higher amplitudes and deviates from the results of the nonlinear FOM by up to -14.57%, which indicates that nonlinear effects become apparent for higher deformations. The mean value of the converged vibrations for case 2 also differs slightly between the linear and nonlinear FOM, namely by 0.9%, and a small phase shift can be observed.

When applying the force correction methods on the nonlinear FOM, the initial deformation becomes larger as expected, and also the amplitudes become higher for case 1, for which the c_{l_α}-correction is applied, and smaller for case 2, in which the polar corrections are used. This comparison of the different modeling capabilities shows the necessity of the nonlinear model and applied force corrections for simulation accuracy for the Delft-Pazy wing model. This is further investigated by looking at one period of these converged results and the experimental deformation measurements as shown in Fig. 10 for both cases at spanwise positions of $y/b = 0.9$. The displayed gust velocity corresponds to the gust velocity at the quarter chord of the wing.

For case 1, the experimental mean deflection of the structure at $y/b = 0.9$ is $z/b = 0.074$ and the amplitude $\Delta z/b = 0.017$. Without any sectional force correction applied, both mean and amplitude are underestimated by -14.31% and -5.81%, respectively, by the nonlinear aeroelastic solver, as expected from the observations made in the previous sections. The polar correction results in both high mean and amplitude error of 10.82% and 29.74%, respectively. The c_{l_α} correction, shown in Fig. 10a, leads to a small overestimation of the mean and amplitude value by 0.79% and 4.02%, respectively.

For case 2, a mean deflection $z/b = 0.140$ and an amplitude $\Delta z/b = 0.071$ have been measured for the Delft-Pazy wing at $y/b = 0.9$. The computational results are significantly improved with the polar corrections regarding the mean and amplitude, namely from -12.77% to -1.40% and 13.42% to 6.36%, respectively. The relative deviations of the wingtip displacement for the dynamic and static simulations are summarized in Table 3.

When the sectional force corrections are applied, the dynamic results are improved significantly as well, while the trends are different from what has been observed for the steady results. We would like to emphasize here that the sectional force corrections are quasi-steady corrections, while with reduced frequencies of $k = 0.1$ and $k = 0.055$ for cases 1 and 2, respectively, unsteady aerodynamic characteristics are expected, particularly in case 1, and

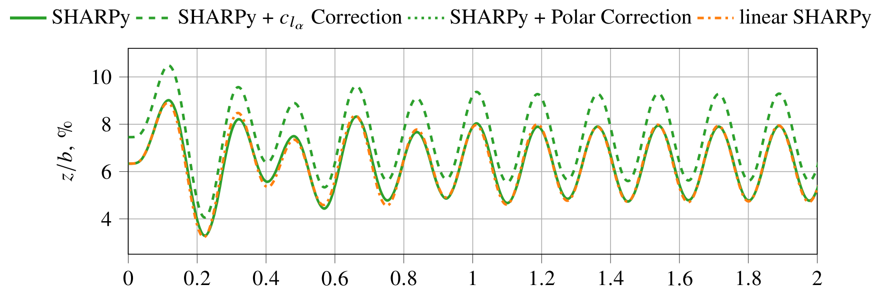

a) Case 1

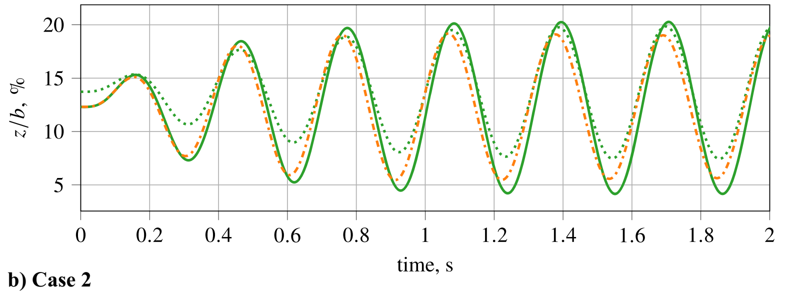

b) Case 2

Fig. 9 Dynamic gust-induced vertical wing deformation at $y/b = 0.9$.

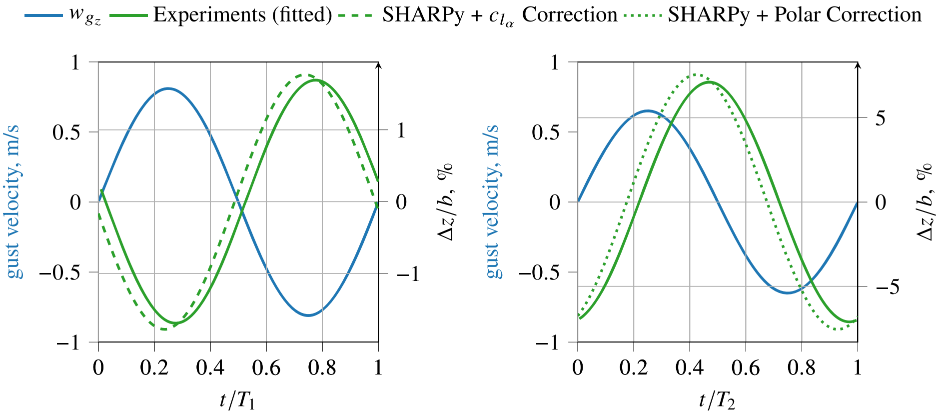

a) Case 1 **b) Case 2**

Fig. 10 Deviation from the mean value of the vertical displacement at $y/b = 0.9$. The reference is the best sinuoisal fit of the experiments from Ref. [5].

Table 3 Relative deviation of the resulting wing tip deflections obtained with SHARPy from the experiments

	Static			Dynamic		
Force correction	α, deg	$\epsilon(z_{\text{tip}})$, %	A_g, m · s^{-1}	f_g, Hz	$\epsilon(\bar{z}_{y/b=0.9})$, %	$\epsilon(\Delta z_{y/b=0.9})$, %
None	5	−14.19	5.7	0.81	−14.31	−5.81
c_{l_α}	5	0.96	5.7	0.81	0.79	4.02
Polar	5	13.05	5.7	0.81	10.82	29.74
None	10	−11.40	3.2	0.65	−12.77	13.42
Polar	10	−1.38	3.2	0.65	−1.4	6.46

unsteady flow separation effects are expected to be present for case 2. These are expected to affect the deviations observed from the dynamic prediction, and more complex data corrections are necessary to improve unsteady computations at low Reynolds numbers with potential flow methods. A different reason, apart from the complexity of the simulation framework, can be erroneous assumptions of the gust input, which will be examined further in the following section.

The experiments in Ref. [5] have also reported a phase shift Φ between the gust, indicated by the blue curve in Fig. 10, arriving at the wing and the observed deformations. The cause of these phase shifts is the response of the harmonically forced dynamic system to the different gust frequencies. The differences between the computationally and experimentally observed phase shifts are considerable, with $\Delta\Phi = -21.5$ deg for case 1 and $\Delta\Phi = -32.1$ deg for case 2. This phase shift is not strongly dependent on the sectional force corrections. With less than 0.2% it is barely affected by the polar and c_{l_α} corrections for case 1. The polar corrections applied to the aerodynamic predictions for case 2 increase the magnitude of the phase shift difference only by 1.11%.

V. Gust Vane Modeling

Instead of using the measured gust as a frozen gust field input, the wake modeling featured by the UVLM enables us to model the gust generated by the gust vanes with a free wake model. To do so, we model the gust vanes, as illustrated in Fig. 11, as lifting surfaces and deflect them by predefined inputs $\delta(t)$, matching the experimental operation conditions, namely maximum gust vane deflections of ±5 deg at frequencies of 5.7 Hz and 3.2 Hz, for cases 1 and 2, respectively. The shed vortex ring panels from these vanes convect downstream and induce velocities on the wing, equivalent to the gust input. The difference from the previously defined gust input is that the singularities distributed on the Delft-Pazy wing and its wake interact with the gust through these induced velocities and their effect on the wake convection. The methods employed do not capture the dissipation of the wake from the gust vanes, whose impact is assessed here.

These interferences between gust and wing are neglected using the frozen turbulence model. In this section, we intend to explore the effect of the frozen turbulence assumption on the gust prediction. In addition, we investigate the local influence of the present wing on the gust, as this might have caused erroneous gust measurements in the experiment. Finally, we explore the stratification of the gust in the vertical direction and its impact on a very flexible wing.

The size of chordwise panels of the lattice grid of the gust vanes is matched to the discretization of the wing to ensure $\mathrm{CFL} = 1$ for the wake shedding at all surfaces. If the vanes are too coarsely discretized, resulting in a CFL number greater than one, the wake convection has been shown not to reflect the actual physical behaviors accurately. The gust vanes' half-wing span is designed to be 10 times larger than that of the Delft-Pazy wing, preserving two-dimensional flow conditions near the center. The spanwise discretization uses 40 vortex ring panels to achieve a stable and converged velocity field. To avoid numerical instabilities caused by the interaction between the wakes of the two structures, the length of the wake behind the vanes is set to $50c$, significantly longer than the Delft-Pazy wing's wake length of $20c$.

A. Local Influence of the Wing on Gust Measurements

We first simulate the gust vanes without the Delft-Pazy wing and compute the induced velocities using Eq. (2) upstream of the wing position, more precisely at $x/c = -0.75$, matching the experimental gust measurement point. The resulting induced velocity oscillations at this location are higher than those measured in the experiments: 1.0 m/s instead 0.81 m/s for case 1 and 0.78 m/s instead of 0.65 m/s for case 2 (23% and 20% higher, respectively). This observed overprediction compares well with the differences observed in the induced velocities from gust vane obtained using UVLM [8] and viscous CFD simulations [9].

The likely reason for these discrepancies is the absence of dissipation modeling in the potential flow model, which may be compounded with the blockage in the wind tunnel. The gust vanes are still useful for exploring interference effects, particularly focusing on gust measurements obtained within the Delft-Pazy experiments. To further investigate this interference, we simulate the gust vanes simultaneously with the current Delft-Pazy wing model. After achieving a convergent dynamic response, the induced velocities at the position of the gust measurements ($x/c = -0.75$) are extracted. We can decompose the contribution of the individual sources to the induced velocity and thus identify the individual influence of the shed vortices of the gust vanes and the wing vortices on the overall velocity field. The induced velocities depend on the circulation of these vortices, which cannot be corrected with the sectional force corrections.

The resulting amplitude of the induced velocity oscillations is presented in Fig. 12 for both cases, once considering only the vortices of the gust vanes and their wakes, and second with all vortex ring panels considered. Hence, the difference between the blue and orange curves stems from the local influence of the wing itself. The leading edge of the wing is at $x/c = 0$, and upstream of the wing, we can observe an exponential increase in the induced-velocity amplitude because of the decreasing distance to the vortex ring panels. At the gust measurement point, the interference effect for both cases is still significant, indicating an overprediction of the gust amplitude by 29.34% for case 1 and 24.1% for case 2. For case 1, the local wing influence becomes negligible from $x/c < -2.7$ with a difference less than 0.1%. For case 2, we reach this difference further upstream at $x/c = 3.5$, indicating a frequency dependency.

In addition to the local influence of the wing, we now address the vertical stratification in the induced gust velocities because of the local distance to the gust vane wakes. This vertical stratification is neglected in the commonly used one-dimensional gust input, but may play a role when the wing has a large deflection in the wind tunnel. Figure 13 shows the deviations in the induced gust amplitude at $x/c = -0.75$ along the vertical axis z, which is here normalized by the distance between the vanes, denoted by d_v.

As expected, the induced velocities are higher close to the convecting gust vane wakes. If we compare the simulation of only the gust vanes with the combined Delft-Pazy wing and gust vane one, we see the effect of the wing deflecting the gust vane wakes, which introduces an asymmetric vertical stratification. More precisely, the deformation of the wing toward the positive vertical direction causes especially the upper wake to be deflected upward, thus causing smaller induced velocities than without these interference effects. Also, the stratification depends on the gust frequency, with higher deviations occurring for case 1 than case 2.

We further observe oscillations in the streamwise induced velocity by the gust vanes, which grow closer to the wing. However, the amplitude is less than 0.5% of the freestream velocity since this induced velocity aligns with the flow velocity, and the contribution to the effective gust angle is expected to be negligible.

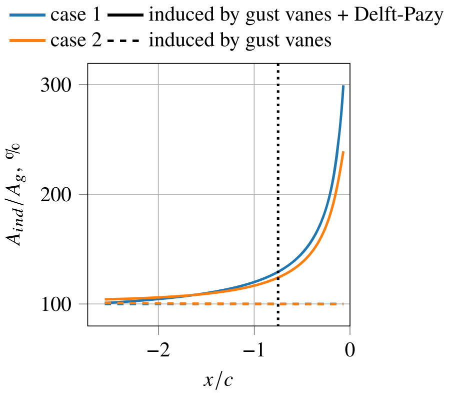

Fig. 12 Streamwise variation in the amplitude of induced velocity oscillations at $z = 0$ upstream the airfoil.

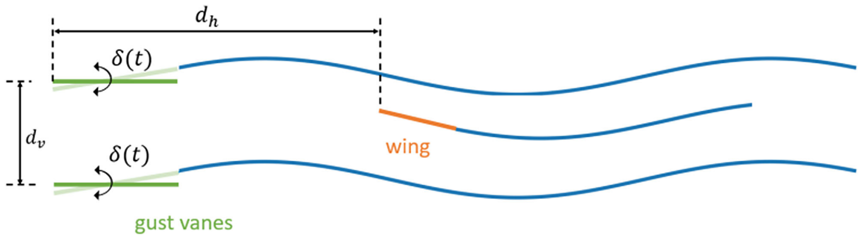

Fig. 11 Two-dimensional illustration of the gust vane modeling simultaneously with the Delft-Pazy wing.

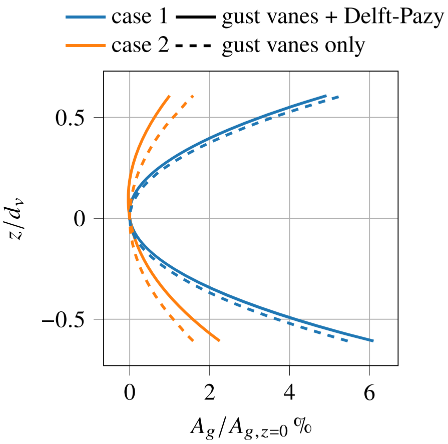

Fig. 13 **Vertical stratification of the relative gust velocity amplitude at $x/c = -0.75$.**

B. Gust Modeling Effect on Deformation Prediction

After analyzing the effect of the gust vane modeling on the velocity field, we investigate next the influence of the computed structural deformations. Therefore, we extract the measured induced velocities by the gust vanes' wakes and use these velocities as a frozen gust input.

The resulting deformations of the converged oscillations are shown in Fig. 14. For both cases, the deformations obtained with the gust vane modeling and the frozen gust input match well. For case 2, these deviations are significantly lower with an error smaller than 0.05% for both mean and amplitude. The effect on the phase shift is also negligible. For case 1, deviations in the mean deformation are only 0.42% but the amplitude deviates by −4.47% and the phase becomes more affected. More notable differences are likely observed in case 1 for the different gust modeling methods because of the more dominant unsteady aerodynamic effects because of the prevailing higher gust frequency.

Note, however, that the results above overpredict those obtained in the experiments due to the absence of the dissipation in the UVLM. For problems where the vane/wing interference may be deemed relevant, a practical solution to this would be to calibrate the gust vane amplitudes such that the desired gust speed amplitudes at the target wing location are achieved.

C. Note on Computational Cost

The simulations are run on a high-performance computer using an AMD EPYC™ 7742 with a clock rate of 2.25 GHz and 50 GB memory, running eight cores in parallel. The simulation time mostly depends on the time steps necessary to achieve converged oscillations. For frozen gust inputs, this is achieved for case 1 after 3500 time steps, while case 2 requires 4500 time steps because of the higher deformations. This results in a CPU time of 19.44 h and 22.49 h or elapsed time of 2.67 h and 3.1 h for cases 1 and 2, respectively. For the gust vane simulation, the computational cost per time step is much higher since we simulate two additional surfaces and, more importantly, two more and much longer wakes. However, since the induced velocities converge quickly, i.e., less than 1000 time steps, the computational time is comparable to the dynamic frozen gust simulations. The combined simulation of gust vanes and Delft-Pazy wing is clearly the most expensive computationally, taking around 7.5 times more than the frozen gust simulations.

VI. Assessment of Nonlinearities

A final question is the extent to which geometrical nonlinearities become apparent in the gust response for the Delft-Pazy wing. As a first test, the nonlinear aeroelastic simulations from Sec. IV (including the force corrections) of the two experimental test cases are computed with the gust amplitude scaled by 1%. For this small amplitude, small deformations and linear dynamics are expected. The resulting converged tip displacement amplitude scales with the original gust amplitude, which indicates that the gust-induced structural dynamics are linear.

To investigate this further and to go beyond the frequencies considered in the experiments, we linearize using the methods of Sec. II.B the Delft-Pazy wing first around its nonlinear aeroelastic equilibria at $\alpha_0 = 5$ deg and $\alpha_0 = 10$ deg. Second, we linearize around the undeformed equilibria, i.e., $\alpha_0 = 0$, to obtain a fully linear model. The simulations in this section consider a horizontally mounted wing and no gravity since the linearization and the gust assembler are only functional for this setup. Also, the force correction methods have only been implemented into the nonlinear aeroelastic solver and are thus not used here. Note that especially due to the missing polar corrections, the tip displacement amplitude is higher for these conditions than before.

The first step is to check the linearity of all three models by comparing their response to a small amplitude gust for which 1% of the experimental gust velocities are used with the frequencies of 5.7 Hz and 3.2 Hz with the nonlinear aeroelastic results. Each linear FOM is compared to the nonlinear results obtained from the same angle of attack it is linearized around. Starting with a frequency of 5.7 Hz, we obtain an excellent match between nonlinear and linear results regarding the resulting tip displacement amplitudes of the converged oscillations with errors of less than 0.5% for the fully linear FOM and the linear FOM, linearized around its equilibrium at $\alpha_0 = 5$ deg. Their transient response following the gust onset is captured perfectly as well. For the FOM, linearized around $\alpha_0 = 10$ deg, the converged amplitudes deviate slightly with 1.20%. For a frequency of 3.2 Hz, we observe for the FOM, linearized around $\alpha_0 = 10$ deg, a constant offset in the gust amplitudes by 7.77%. Amplitude deviations of

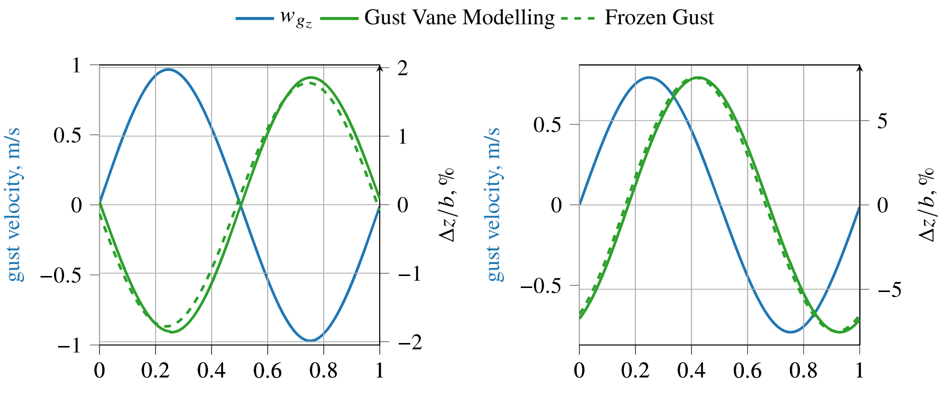

a) Case 1 **b) Case 2**

Fig. 14 **Dynamic vertical wing deflection at $y/b = 0.9$ for different gust models.**

1.57% and −2.72% result for the fully linear FOM and the FOM, linearized around $\alpha_0 = 5$ deg.

Next, we compute the expected oscillated wingtip displacement amplitudes for the different gust amplitudes for frequencies in the range from $f_g = 1$ Hz to $f_g = 5.8$ Hz using the linear FOMs. The amplitudes are normalized by the gust amplitude and are displayed in Fig. 15. The peak in the wingtip displacement amplitude is attributed to the first (OOP) bending mode. The frequency of this mode varies for the different linear FOMs as the modal frequencies shift slightly with wing deformation, as observable in Fig. 16. This figure contains the modal frequencies of the first five modes as a function of their nonlinear static deformation due to different flow velocities and angles of attack. The first five modes for the undeformed wing ($z/b = 0$) are the same as identified in Table 2, i.e., OOP1, OOP2, T1, OOP3, IP1, and T2. With increasing wing deformation, the natural frequencies change, especially the first torsional mode that crosses the second OOP bending mode at around $z/b = 0.28$ as well as a significant drop of the first in-plane bending mode from 107.40 Hz to almost 40 Hz while crossing the third OOP bending mode. These mode switches have also been observed for the Technion Pazy [1].

The natural frequencies of the OOP bending modes change much less. However, a zoom-in of the first mode shows a general higher frequency for higher angles of attack with the same deformation as well as the slight increase of the frequency with deformation up to $y/b = 0.18$ for $\alpha = 5$ deg and $y/b = 0.34$ for $\alpha = 10$ deg. These deformations are not exceeded, neither in the static deformation nor in the dynamic deformation with gust-induced amplitudes of $y/b = 0.17$ and $y/b = 0.22$ for $\alpha = 5$ deg and $\alpha = 10$ deg, respectively. The difference in the natural frequency for the different angles of attack seems to match the ones observed in Fig. 15, although for $\alpha_0 = 10$ deg, the resonance frequency seems to be more accurately predicted with the nonlinear FOM.

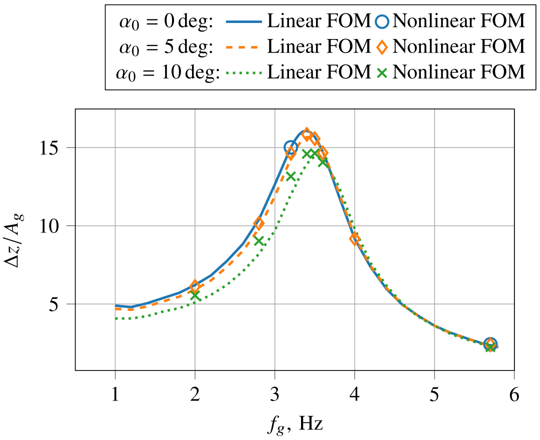

Fig. 15 Wingtip displacement amplitude over various gust frequencies.

The peak amplitude in Fig. 15 further reduces with the linear FOM, which is linearized for increasing angles of attack due to geometrical stiffening at higher deformations. Although the three linear FOMs converge to similar wingtip displacement amplitudes at higher frequencies, a noticeable difference between the FOMs is evident at frequencies lower than the first modal frequency. While for frequencies higher than this frequency all FOMs converge to the same wingtip displacement from around $f_g = 4$ Hz, an offset between the FOMs can be observed for decreasing frequencies.

We continue with examining the extent of geometrically nonlinear effects becoming apparent for different frequencies, as there is clearly a dependency observable. Therefore, we compute with the nonlinear FOM the resulting wingtip displacement amplitudes for different combinations of gust frequencies f_g and amplitudes A_g. The results obtained with a gust amplitude of $A_g = 0.65$ m/s are marked in Fig. 15. If we excite the Delft-Pazy wing with a sinusoidal gust in the undeformed state, the wingtip deformation amplitudes obtained with the nonlinear FOM match the linear results for the frequencies of 3.2 Hz and 5.7 Hz with less than a deviation of 1%. However, a fully linear FOM is not sufficient in predicting the results of the moderately large steady deflections of the Delft-Pazy model.

VII. Conclusions

This work has investigated the nonlinear aeroelastic simulation of the dynamic gust response of very flexible wings. As a reference for assessment, the highly flexible Delft-Pazy wing was used. This wing has been experimentally tested at the Delft University of Technology in unsteady aerodynamic inflow conditions and moderately large structural deformations. For this study, a numerical model of this wind tunnel wing was implemented into the open-source `SHARPy` framework.

First, we have computed the steady and dynamic gust-induced deformations corresponding to the wind tunnel conditions and compared the instantaneous structural deformations with the experimental results. For the steady case, excellent agreement was achieved for deflections of up to 24% of the wingspan by applying sectional force corrections to account for the low Reynolds number and stall onset effects, which are not captured by potential flow theory. It was found that different types of corrections are needed for different angles of attack, possibly because of the high shape distortions in this wing. For the dynamic case, the prediction of the deformation amplitudes also matches well with the experiments for additional deflections of up to 5% of the wingspan. Small deviations are observed for the two cases that were analyzed, which can be mainly explained by the quasi-steady force correction methods applied on an unsteady aeroelastic problem, as well as inaccuracies

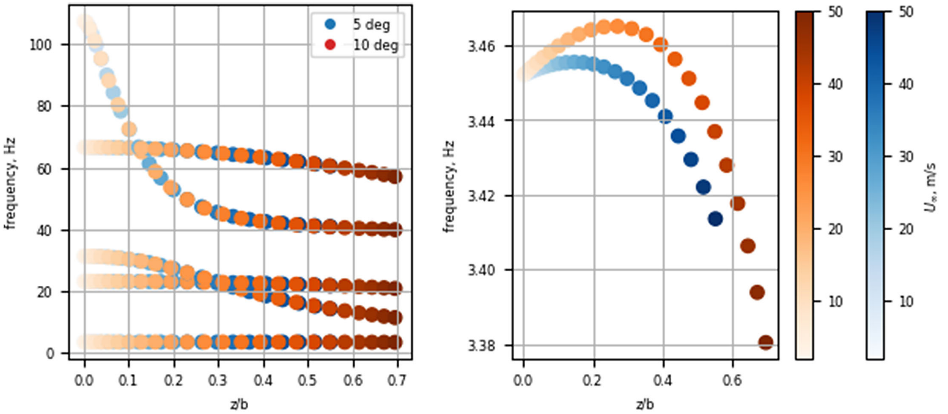

a) First to fifth mode

b) First mode

Fig. 16 Frequencies of the first five modes changing with wing deformation.

in the frozen gust velocity input, which was therefore further investigated.

This frozen gust velocity input originated from flowfield measurements done in the wind tunnel experiments upstream of the wing, with the wing installed. The local influence of the wing on the gust measurement was thus investigated and quantified in this work by simulating the gust vanes simultaneously with the Delft-Pazy wing. The obtained results indicate an overprediction of the gust measurements obtained at the gust measurement point, while the influence of the wing becomes fully negligible only much further upstream of the wing. Since modeling the gust vanes with potential flow methods overpredicts the gust velocity in general, a direct quantification of the resulting error cannot be given. We further used this gust vane modeling to explore possible limitations of the frozen gust model. While for the second test case with larger deflections, the deviations in the structural response are negligible, and we observed slight deviations for the first case for which unsteady aerodynamic effects are more relevant because of the higher gust frequency.

Lastly, this work has explored the relative importance of geometric nonlinearities in the dynamic gust responses. For this purpose, nonlinear aeroelastic simulations were performed for different gust frequencies and amplitudes. These results indicate that nonlinear effects are relevant but only stem from the nonlinear aeroelastic equilibrium and not the gust excitation, even with the largest deflections considered that appear when targeting specifically the excitation of the first out-of-plane bending mode.

It needs to be remarked that the need for a different correction method at each angle of attack is an undesirable feature of the current approach, but it is a pragmatic solution given that alternative strategies were available to tackle an nonstandard problem. The experiments were on a highly flexible wing that also had very deformable airfoils. A fully predicted capability would need to either use high-fidelity formulations for both fluid and structure or provide a full 3D scan of the deformed wing in the wind tunnel. Neither of those was available for this work.

In summary, the aspects of gust response predictions for flexible wings that were investigated in the presented work are relevant for future studies when considering the definition of further combined experimental–numerical campaigns that aim at improving the accuracy of medium-fidelity tools, such as those used in this work. This could be achieved with a follow-up study analyzing nonlinear aeroelastic effects over various ranges of gust-induced deformation amplitudes and frequencies. Ultimately, this is of interest for the potential use of such cost-efficient modeling tools early on in the design process of future aircraft incorporating ultra-high-aspect-ratio wings.

Acknowledgments

The experimental work reported in this paper has been carried out in the context of the ”Holistic Optical Metrology for Aero-Elastic Research” project, which has received funding from the European Union’s Horizon 2020 Research and Innovation Programme under Grant Agreement No. 769237. The authors would like to thank Cristina Riso for the structural beam model of the Delft-Pazy wing and acknowledge the contributions of J. L. Costa Fernández, A. Grille Guerra, J. Sodja, A. Sciacchitano, and B. W. van Oudheusden from Delft University of Technology to the acquisition, processing, and analysis of the experimental data.

References

[1] Ritter, M., Hilger, J., Ribeiro, A., Öngüt, A. E., Righi, M., Raveh, D. E., Drachinsky, A., Riso, C., Cesnik, C. E., Stanford, B., et al., “Collaborative Pazy Wing Analyses for the Third Aeroelastic Prediction Workshop,” *AIAA SciTech 2024 Forum*, AIAA Paper 2024-0419, 2024.
https://doi.org/10.2514/6.2024-0419

[2] Avin, O., Raveh, D. E., Drachinsky, A., Ben-Shmuel, Y., and Tur, M., “Experimental Aeroelastic Benchmark of a Very Flexible Wing,” *AIAA Journal*, Vol. 60, No. 3, 2022, pp. 1745–1768.
https://doi.org/10.2514/1.J060621

[3] Drachinsky, A., Avin, O., Raveh, D. E., Ben-Shmuel, Y., and Tur, M., “Flutter Tests of the Pazy Wing,” *AIAA Journal*, Vol. 60, No. 9, 2022, pp. 5414–5421.
https://doi.org/10.2514/1.J061717

[4] Palacios, R., and Cesnik, C. E. S., *Dynamics of Flexible Aircraft: Coupled Flight Mechanics, Aeroelasticity, and Control*, Cambridge Aerospace Series, Cambridge Univ. Press, Cambridge, England, U.K., 2023.
https://doi.org/10.1017/9781108354868

[5] Mertens, C., Costa Fernández, J. L., Sodja, J., Sciacchitano, A., and van Oudheusden, B. W., “Nonintrusive Experimental Aeroelastic Analysis of a Highly Flexible Wing,” *AIAA Journal*, Vol. 61, No. 7, 2023, pp. 3062–3077.
https://doi.org/10.2514/1.J062476

[6] Mertens, C., de Rojas Cordero, T., Sodja, J., Sciacchitano, A., and van Oudheusden, B. W., “Aeroelastic Characterization of a Flexible Wing Using Particle Tracking Velocimetry Measurements,” *AIAA Journal*, Vol. 60, No. 1, 2022, pp. 276–286.
https://doi.org/10.2514/1.J060713

[7] Ribeiro, A. F., Casalino, D., and Ferreira, C., “Free Wake Panel Method Simulations of a Highly Flexible Wing in Flutter and Gusts,” *Journal of Fluids and Structures*, Vol. 121, 2023, Paper 103955.
https://doi.org/10.1016/j.jfluidstructs.2023.103955

[8] Kassem, A. V., “Wind Gust Generation for Wind Turbine Testing via Numerical Methods,” Master’s Thesis, TU Delft, Delft, The Netherlands, 2010.

[9] Lancelot, P., Sodja, J., Werter, N., and De Breuker, R., “Design and Testing of a Low Subsonic Wind Tunnel Gust Generator,” *Advances in Aircraft and Spacecraft Science*, Vol. 4, No. 2, 2017, pp. 125–144.
https://doi.org/10.12989/aas.2017.4.2.125

[10] del Carre, A., Muñoz-Simón, A., Goizueta, N., and Palacios, R., “SHARPy: A Dynamic Aeroelastic Simulation Toolbox for Very Flexible Aircraft and Wind Turbines,” *Journal of Open Source Software*, Vol. 4, No. 44, 2019, p. 1885.
https://doi.org/10.21105/joss.01885

[11] Géradin, M., and Cardona, A., *Flexible Multibody Dynamics: A Finite Element Approach*, Wiley, Hoboken, NJ, 2001.

[12] Simpson, R. J., and Palacios, R., “Numerical Aspects of Nonlinear Flexible Aircraft Flight Dynamics Modeling,” *54th AIAA/ASME/ASCE/AHS/ASC Structures, Structural Dynamics, and Materials Conference*, AIAA Paper 2013-1634, 2013.
https://doi.org/10.2514/6.2013-1634

[13] Goizueta, N., Wynn, A., and Palacios, R., “Adaptive Sampling for Interpolation of Reduced-Order Aeroelastic Systems,” *AIAA Journal*, Vol. 60, No. 11, 2022, pp. 6183–6202.
https://doi.org/10.2514/1.J062050

[14] Shearer, C., and Cesnik, C., “Modified Generalized Alpha Method for Integrating Governing Equations of Very Flexible Aircraft,” *47th AIAA/ASME/ASCE/AHS/ASC Structures, Structural Dynamics, and Materials Conference*, AIAA Paper 2006-1747, 2006.
https://doi.org/10.2514/6.2006-1747

[15] Murua, J., Palacios, R., and Graham, J. M. R., “Applications of the Unsteady Vortex-Lattice Method in Aircraft Aeroelasticity and Flight Dynamics,” *Progress in Aerospace Sciences*, Vol. 55, 2012, pp. 46–72.
https://doi.org/10.1016/j.paerosci.2012.06.001

[16] Morino, L., and Bernardini, G., “Singularities in BIEs for the Laplace Equation; Joukowski Trailing-Edge Conjecture Revisited,” *Engineering Analysis with Boundary Elements*, Vol. 25, No. 9, 2001, pp. 805–818.
https://doi.org/10.1016/S0955-7997(01)00063-7

[17] Katz, J., and Plotkin, A., *Low-Speed Aerodynamics*, Vol. 13, Cambridge Univ. Press, Cambridge, England, U.K., 2001.
https://doi.org/10.1017/CBO9780511810329

[18] Simpson, R. J., Palacios, R., and Murua, J., “Induced-Drag Calculations in the Unsteady Vortex Lattice Method,” *AIAA Journal*, Vol. 51, No. 7, 2013, pp. 1775–1779.
https://doi.org/10.2514/1.J052136

[19] Düssler, S., and Palacios, R., “Enhanced Unsteady Vortex Lattice Aerodynamics for Nonlinear Flexible Aircraft Dynamic Simulation,” *AIAA Journal*, Vol. 62, No. 3, 2024, pp. 1179–1194.
https://doi.org/10.2514/1.J063174

[20] Maraniello, S., and Palacios, R., “State-Space Realizations and Internal Balancing in Potential-Flow Aerodynamics with Arbitrary Kinematics,” *AIAA Journal*, Vol. 57, No. 6, 2019, pp. 2308–2321.
https://doi.org/10.2514/1.J058153

[21] Mertens, C., Sciacchitano, A., van Oudheusden, B. W., and Sodja, J., "An Integrated Measurement Approach for the Determination of the Aerodynamic Loads and Structural Motion for Unsteady Airfoils," *Journal of Fluids and Structures*, Vol. 103, No. 103293, 2021, Paper 103293. https://doi.org/10.1016/j.jfluidstructs.2021.103293

[22] Sanghi, D., Riso, C., and Cesnik, C., "Evaluation of Aeroelastic Models for Gust Response Prediction in Very Flexible Wings," *International Forum on Aeroelasticity and Structural Dynamics*, IFASD, Hague, Netherlands, 2024.

[23] Riso, C., and Cesnik, C. E., "Correlations Between UM/NAST Nonlinear Aeroelastic Simulations and the Pre-Pazy Wing Experiment," *AIAA Science and Technology Forum and Exposition*, AIAA Paper 2021-1712, 2021. https://doi.org/10.2514/6.2021-1712

[24] Goizueta, N., Wynn, A., Palacios, R., Drachinsky, A., and Raveh, D. E., "Flutter Predictions for Very Flexible Wing Wind Tunnel Test," *Journal of Aircraft*, Vol. 59, No. 4, 2022, pp. 1082–1097. https://doi.org/10.2514/1.C036710

[25] Eggert, C. A., and Rumsey, C. L., "CFD Study of NACA0018 Airfoil with Flow Control," NASA TM 219602, Langley Research Center, Hampton, VA, 2017.

[26] Fehrs, M., Ritter, M. R., Helm, S., and Mertens, C., "CFD Simulations of the Pazy Wing in Support of the Third Aeroelastic Prediction Workshop," *International Forum on Aeroelasticity and Structural Dynamics*, IFASD, Madrid, Spain, 2022.

T. Strganac
Associate Editor